Structural and optical investigation of novel $Sr_{1-x}Na_{2x}ZrO_3$ perovskite nanoparticles

A. Nathan-Abutu [a,b], I. Ahemen [b], A. Reyes-Rojas [a,*]

[a] *Materials Science Department. Centro de Investigacion' en Materiales Avanzados, S.C., Miguel de Cervantes 120, Complejo Industrial Chihuahua, 31109, Chihuahua, CHIH, Mexico*
[b] *Department of Physics, Federal University of Agriculture, P.M.B. 2373, Makurdi, Benue State, Nigeria*

ARTICLE INFO

ABSTRACT

Novel $Sr_{1-x}Na_{2x}ZrO_3$ ($0 \leq x \leq 0.4$) perovskite nanoparticles have been fabricated via the citrate-ethylene glycol sol-gel route and systemically studied. The XRD analysis shows $Sr_{1-x}Na_{2x}ZrO_3$ crystallized in orthorhombic structure, Rietveld refinement analysis revealed that Na ion acts positively to prevent large distortion of the perovskite, with a cell-volume contraction compared to the pure $SrZrO_3$. Raman spectral results confirmed the existence of minor impurities. Besides, the calculated low phonon energy of 442 cm^{-1} makes $Sr_{1-x}Na_{2x}ZrO_3$ perovskite a promising host matrix for phosphor-based photonic applications. The decrease in the optical band gap (E_{gap}) from 4.85 eV to 4.42 eV is link to the formation of localized states in the band gap due to lattice disorder and oxygen vacancies. Photoluminescence results revealed broad band emissions in the range 300–800 nm as a result of transitions involving multiple relaxation paths. The $Sr_{1-x}Na_{2x}ZrO_3$ perovskite is a promising candidate for phosphor host matrix.

1. Introduction

A reliable energy supply is critical for lighting, heating, communications, computers, industrial equipment, transportation and more in the global economy (IEA 2021) [1]. However, the growing global population and the need for humans to explore the universe have created a huge gap between available energy and the required energy. Traditional ways of bridging this energy gap have fallen short of the required standards, so there is a need to find more affordable, efficient, and more abundant environmentally friendly energy sources. Over the past several years, inorganic metal halide perovskites (IMHP) materials have become one of the most sought, investigated, and exciting material systems because of their low cost, high redox and thermal stability, structural stability at high temperatures, the tunability of light emission, etc. [2–5]. But, related to halide-perovskite is the challenge of low quantum efficiency at high charge carrier density due to the strong Auger recombination [6,7]. All-inorganic perovskites have low non-radiative recombination rates; thus, may exhibit higher efficiencies [7].

Several studies have shown that perovskites can be directly translated into high-performance device applications such as high-efficiency light-emitting diodes (LEDs) [8–12], solar cells [[13,14]], lasers [[15,

16]], photodetectors [[17,18]] etc. Perovskite materials also have a flexible property whereby their bandgap can be tuned simply by adjusting or controlling the perovskite geometry (which involves changes in the temperature and substitutions in A, B, and X components) [19] to activate color changes from one wavelength to another within the electromagnetic spectrum. From the context of LEDs synthesis and fabrication, this means that multi-color systems such as white light are achievable by a combination of chemicals [20–22].

As an inorganic oxide perovskite material, $SrZrO_3$ exhibits excellent electrical and thermomechanical properties with high-temperature properties up to 2600 °C [23], with little phase transition and mass loss. These properties lead to their applications in solid oxide fuel cells [24–26], optical coatings, gas sensors, proton conductivity, catalysts, luminescent materials, refractories, etc. [27–33]. Considering the lattice dimension of $SrZrO_3$, this compound contains divalent Sr^{2+} and tetravalent Zr^{4+} ions. This fact is a good indication that when a monovalent element such as Na^+ is incorporated at either of the two lattice sites, there will be charge compensation from intrinsic defects such as vacancies. Besides, the size difference between Na^+ and the site cations means there could be a slight distortion in the lattice thereby lowering the site symmetry and enhancing luminescence if doped with rare-earth ions.

Table 1
Chemicals used in the synthesis of $Sr_{1-x}Na_{2x}ZrO_3$.

Chemical	Molecular formula	Manufacturer	Purity (%)
Sodium Nitrate	$NaNO_3$	Sigma-Aldrich, USA	99.999
Strontium Nitrate Anhydrous	$Sr(NO_3)_2$	Fisher Scientific, USA	99.70
Zirconium (IV) 2,4-pentanedionate	$ZrC_{20}H_{28}O_8$	Alfa Aesar, Thermo Fisher Scientific, USA	99.72
Citric Acid monohydrate	$C_6H_8O_7.H_2O$	J.T. Baker, Mexico	99.5–100.5
Ethylene Glycol (ethane-1,2-diol)	$C_2H_6O_2$	J.T. Baker, Mexico	≥99

The physicochemical properties of the $SrZrO_3$ lattice are enhanced by the dopant interaction, which is observed from several studies with different dopants: for example, $SrZrO_3:Sm^{3+}/Dy^{3+}$ [34], displayed characteristic emissions of Sm^{3+} and Dy^{3+}; $SrZrO_3:Eu^{3+}$ [35–37] phosphor show an enhanced microstructure and orange-reddish emission from the rare-earth ion; $SrZrO_3:Ge$ [38] showed better improved atomic and electronic properties; $SrZrO_3:Gd^{3+}$ [39,40] exhibited better paramagnetic, luminescence and solid fuel oxide properties over the pure sample; also for $(SrZrO_3)_{1-x}Cu_x$ [41], Cu ion doping lead to the formation of more mid-gap states as deep acceptor within the band gap of $SrZrO_3$, which is responsible for the red and green emission; In $SrZr_{1-x}Al_xO_{3-\delta}$ [24], the Al^{3+}-doping exhibits excellent thermal stability below 1400 °C than the undoped sample; Similarly, the spectroscopic probe of $LiY_xSr_yZrO_{3+\alpha}:Eu^{3+}$ [42] revealed the presence of two possible sites for the Eu^{3+} ions with the dopant preferentially occupying the more symmetric (less distorted) Sr^{2+} sites; Sedeek et al. [43] observed a decrease in the optical band gap width from 4.40 eV to 4.21 eV by La incorporation into $SrZrO_3$ due to the presence of defect states such as oxygen and strontium vacancies; in $SrZr_{0.9}Y_{0.1}O_{2.95}$ [44], high temperature treatment resulted in a maximum proton solubility of about 0.04 mol/mol compound with clear evidence for proton conduction. The conductivity of protonated samples was found to increase linearly with the proton content because of the yttrium incorporation into the B-site of $SrZrO_3$ lattice.

For the above reasons and others that may be obvious, this study aims to introduce a novel $Sr_{1-x}Na_{2x}ZrO_3$ perovskite nanocrystalline materials. Like Li^+ [42], we expect Na ions to contribute to the enhancement of the crystal structure and the band gap tuning of the $SrZrO_3$ structure. Therefore, compared with pure $SrZrO_3$ perovskite, $Sr_{1-x}Na_{2x}ZrO_3$ perovskite should have smaller crystallites and more cation-oxygen bonds, resulting in higher oscillation intensity of optical transitions within doped ions. The incorporation of Na into $SrZrO_3$ crystals should slightly alters the local crystal field (local symmetry) and

ion pairing of $SrZrO_3$. Moreover, incorporating Na ions should also create oxygen vacancies that can improve energy transfer to the activator. To the best of our knowledge, this is the first time that $Sr_{1-x}Na_{2x}ZrO_3$ perovskite nanoparticles have been studied and prepared by a citrate-ethylene glycol sol-gel synthesis technique and reported in an academic journal. The closest perovskite to $Sr_{1-x}Na_{2x}ZrO_3$ perovskite is the $(Na_{0.5}Bi_{0.5})ZrO_3$ perovskite first published by Smolenskii in 1961 [45].

2. Experimental details

Sodium-doped strontium zirconate $[Sr_{1-x}Na_{2x}ZrO_3 \ (0 \leq x \leq 0.4)]$ perovskite nanocrystals were prepared by a one-step citrate-ethylene glycol sol-gel method using the chemicals/reagents listed in Table 1. All reagents were of analytical grade and used as provided without further purification. Stoichiometric amounts of sodium nitrate, strontium nitrate, and zirconium (IV) 2,4-pentanedionate were dissolved in 60 ml of distilled water under constant stirring and controlled temperature (70 °C) for 2 h; subsequently, citric acid was added to the obtained mixed solution at a molar ratio of 2:1 (citric acid: a metal ion) and again stirred uniformly for another 1 h. After the dissolution of citric acid, ethylene glycol was added dropwise to the mixture as a gel stabilizer; (the molar ratio of metal cations and ethylene glycol was 1:3). The final solution was heated at 70 °C with continuous stirring until the precursor solution was gelatinous. The xerogel was left to dry at 80 °C for 12 h.

The dried xerogel was transferred to a ceramic crucible and preheated at 400 °C for 2 h. The preheated black residual powder was properly ground and post-annealed at 1050 °C for 4 h at a heating rate of 5 °C/min; the obtained solids were pulverized to a fine powder and stored for various characterization.

The phase composition and crystallographic identification of $Sr_{1-x}Na_{2x}ZrO_3$ perovskite powders were determined from an Empyrean diffractometer from PANalytical-Xpert powder X-ray diffractometer equipped with Cu-kα radiation of $\lambda = 0.15418$ nm at 40 kV and 30 mA; scanning rate of 0.01°/s at 2θ range between 10° – 80°. The Full-Prof_suite software was used to perform Rietveld refinement of the XRD powder patterns. Thermogravimetric analysis (TGA) and differential scanning calorimeter (DSC) measurements were carried out on the samples using the Q50 TGA Thermogravimetric Analyzer 953,501 system in a temperature range of 0 °C–900 °C at a heating rate of 10 °C/min. Morphology and grain size distribution of nanoparticles were analyzed using a Hitachi SU3500 Scanning Electron Microscope (SEM) with an energy dispersive spectrometer (EDS) attachment. The UV–Vis absorption spectra data were obtained using a Shimadzu UV-1280 UV–Vis spectrophotometer. The infrared emissivity was studied with the help of an AIM-9000 Fourier transform infrared (FTIR) spectrometer
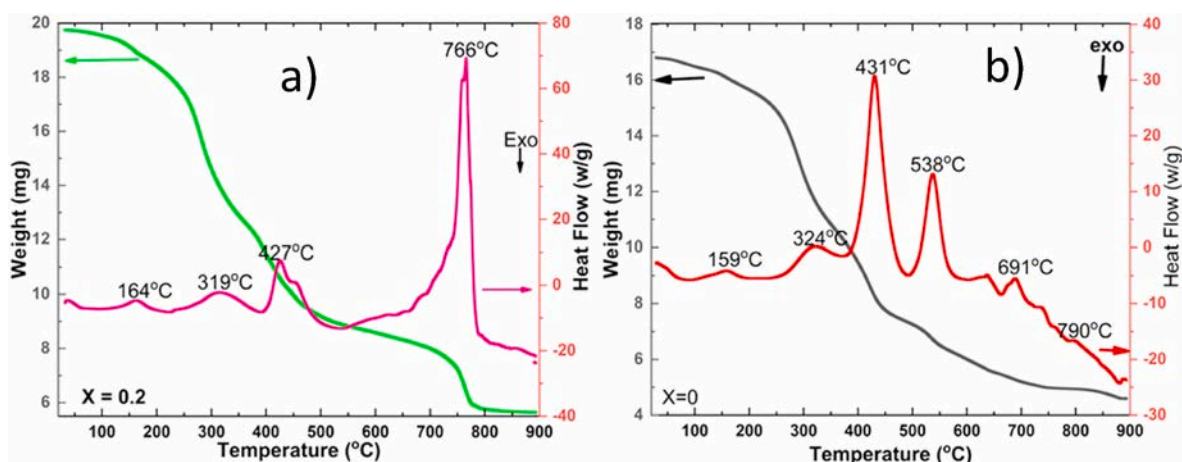

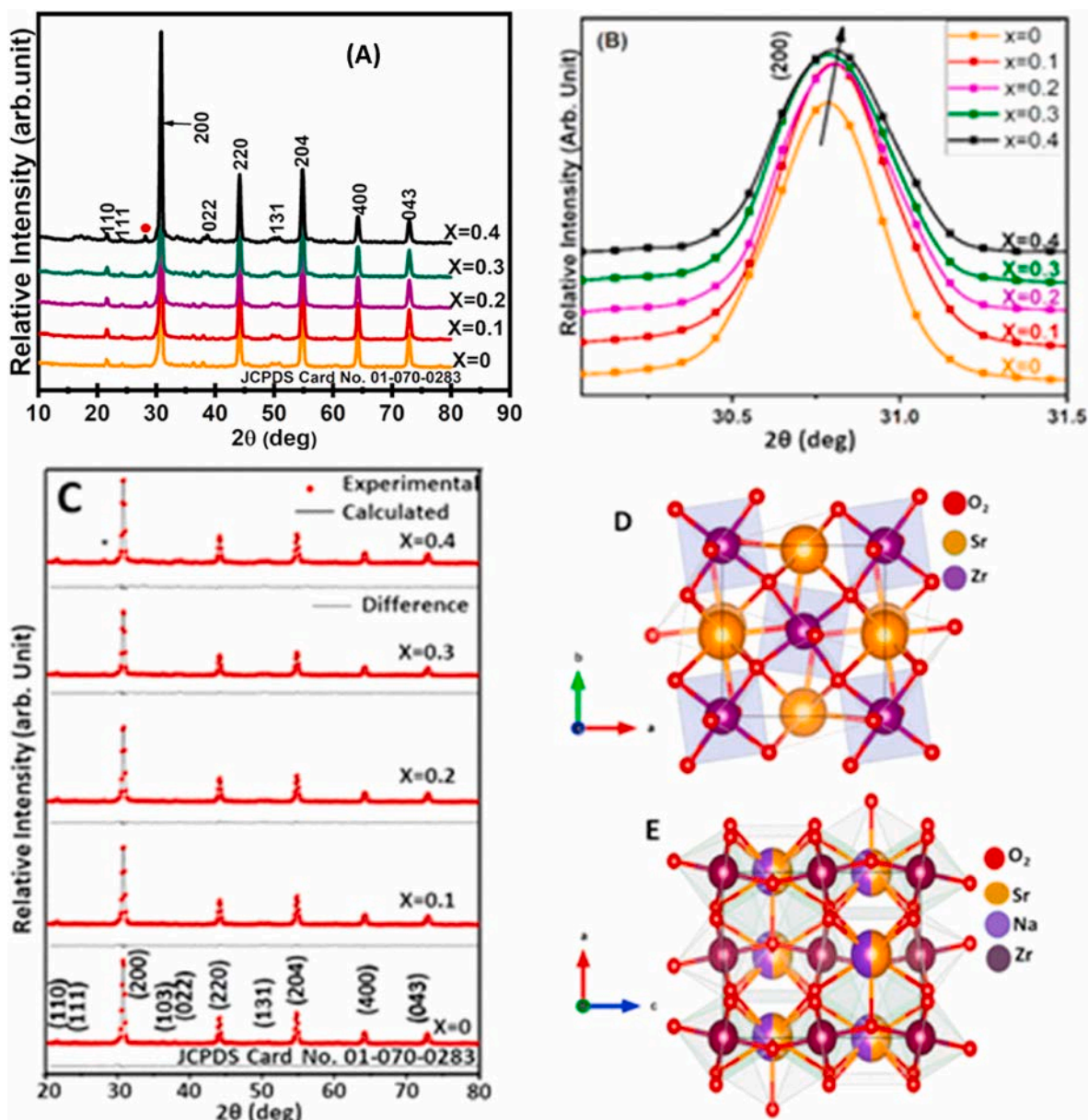**Fig. 1.** TGA-DSC curves of (a) $SrZrO_3$ and (b) $Sr_{0.9}Na_{0.2}ZrO_3$ perovskite nanoparticles.

Fig. 2. **(A)** X-ray diffraction pattern, **(B)** peaks shift and **(C)** Rietveld analysis, **(D and E)** packing diagram for $SrZrO_3$ and $Sr_{0.9}Na_{0.2}ZrO_3$) perovskite nanocrystals.

in the wave number region 4000 cm^{-1} to 400 cm^{-1}. Raman spectroscopy experiment was carried out using an XploRA INV-Horiba inverted Raman microscope. Photoluminescence spectra were collected using a He–Cd laser PL system with a 325 nm excitation wavelength. All the aforementioned measurements are at room temperature.

3. Results and discussions

3.1. Thermal (TGA-DSC) analysis

Fig. 1a and a shows the TGA-DSC curves of pure $SrZrO_3$ and $Sr_{1-x}Na_{2x}ZrO_3$ perovskites, respectively. Three distinct phases of the weight loss were observed in the spectra of all samples. The first stage between 100 and 250 °C presents a weight loss of ~11.1% and ~11.5% for $SrZrO_3$ perovskites (Fig. 1a) and $Sr_{1-x}Na_{2x}ZrO_3$ perovskite (Fig. 1b), respectively. The weight loss is attributed to the dehydration of the samples. The second stage in the range 250 °C–521 °C for $SrZrO_3$ perovskite and 250 °C–732 °C for $Sr_{1-x}Na_{2x}ZrO_3$ perovskite with ~47% and ~50% weight losses is attributed to the decomposition of residual

organics such as citric acid and ethylene glycol. The final stage in the range 521 °C–838 °C has ~12.6% weight loss for the $SrZrO_3$ perovskite, and ~9.1% for weight loss $Sr_{1-x}Na_{2x}ZrO_3$ corresponding to the decomposition of nitrates.

In all of the samples, there is close to 70% weight loss. There no observed weight loss above 750 °C and 790 °C for $Sr_{1-x}Na_{2x}ZrO_3$ and $SrZrO_3$ perovskite, respectively, showing a stable oxide formation and also affirming $Sr_{1-x}Na_{2x}ZrO_3$ perovskite is thermally stable at higher temperatures. The inclusion of Na^+ (acting as a flux) influenced the faster decomposition process of the $Sr_{1-x}Na_{2x}ZrO_3$ perovskite as observed from the TGA-DSC curves.

3.2. Structural analysis

Fig. 2A shows the XRD pattern of $Sr_{1-x}Na_{2x}ZrO_3$ perovskite nanoparticles crystallized in the orthorhombic phase of $SrZrO_3$ (*Pbnm*, space group number 62) in accordance with the standard reference JCPDS card number 01-070-0283. The peaks at 2θ values 21.75, 24.15, 30.85, 36.35, 38.65, 44.15, 50.65, 54.75, 64.15 and 72.85° correspond to the

Table 2
Cell parameters (a,b,c) Å; the cell volume (Å^3), tolerance factor and average crystallite sizes (nm) of Sr$_{1-x}$Na$_{2x}$ZrO$_3$.

x	a	b	c	Unit cell Volume	Goodness of Fit	Bond Angle	σ_{JT}	Tolerance factor	Crystallite size
		(Å)		(Å^3)	χ^2	Zr–O2 –Zr	(10^{-2}) (Å)		(nm)
0	5.7939 (1)	5.8177 (1)	8.1951 (2)	276.235 (1)	1.4	158.278	2.1	0.95	20.9
0.1	5.7923 (1)	5.8097 (1)	8.1956 (1)	275.797 (1)	1.5	158.825	3.1	0.99	20.5
0.2	5.7931 (1)	5.8103 (1)	8.1957 (1)	275.868 (1)	1.5	158.122	1.5	1.03	20.5
0.3	5.7915 (1)	5.8139 (1)	8.1949 (1)	275.941 (1)	1.6	157.594	1.3	1.08	19.9
0.4	5.7945 (1)	5.8141 (1)	8.1941 (1)	276.054 (1)	1.7	157.450	1.1	1.12	18.6

(110), (111), (200), (103), (022), (220), (131), (204), (400) and (043) reflections of SrZrO$_3$, respectively. Other weak peaks at 17° (011), 28° (−111), and 34° (200) belonging to the monoclinic phase of ZrO$_2$ were also observed. The presence of the ZrO$_2$ phase in SrZrO$_3$ is a common phenomenon of solid-phase doping at temperatures ≥1000 °C and has a negligible effect on its optical properties [46,47]. The incorporation of Na at the Sr sites of the Sr$_{1-x}$Na$_{2x}$ZrO$_3$ matrix does distort the host lattice slightly. The relative intensities of the characteristic peaks of SrZrO$_3$ reduced and broadened with increasing Na concentration (Fig. 2B). The decrement of peak intensities and broadening might be due to the decrease of the crystallinity, crystallite size as well as increase in the lattice disorder and strain induced by Na$^+$ substitution [38]. The intensity of some of the ZrO$_2$ peaks increased with increasing concentration of Na, while others vanished.

The samples were subjected to Rietveld refinement analysis to determine the exact lattice parameters, assuming the orthorhombic twisted perovskite-type structure of Sr$_{1-x}$Na$_{2x}$ZrO$_3$ with the *Pbnm* space group. The refined structure and lattice parameters are given in Table 2. Both the experimental and calculated XRD parameters by Rietveld refinement of SrZrO$_3$ and Sr$_{1-x}$Na$_{2x}$ZrO$_3$ are in agreement with JCPDS Card No. 01-070-0283, and with other authors [24,48–50]. In Rietveld refinement, the resulting XRD pattern should be minimized, taking into account reliability factors, differences between experimental and theoretical (calculated), and the goodness-of-fit χ^2 value should be 1 [51]. In Table 2, the XRD patterns of the perovskite under review, with a χ^2 of about 1, confirm the good refinement of the XRD analysis.

From the Rietveld refinement results, the unit cell volume of all Na doped samples (Sr$_{1-x}$Na$_{2x}$ZrO$_3$ perovskite) are smaller than the value for undoped sample (SrZrO$_3$ perovskite), indicating lattice shrinkage. The lattice contraction is an indication that a smaller ion (Na$^+$) substituted the bigger ion (Sr^{2+}) in the lattice [52]. The SrZrO$_3$ crystallizes in the ideal A^{2+}B^{4+}O$_3^{2-}$ perovskite structure with the A atom (in this case Sr atom) occupying the corner position with a 12-fold coordination with oxygen atoms to form a SrO$_{12}$ cuboctahedral, and the B atom (Zr atom) sitting at the center of an octahedral where it coordinated by 6-oxygen atoms to form ZrO$_6$ octahedron. The unit cell has the ZrO6 octahedral embedded inside a cube formed by Sr atoms (see the inset in Fig. 2 D and E). On doping Na with SrZrO$_3$, the possible site occupancy of Na in the Sr$_{1-x}$Na$_{2x}$ZrO$_3$ nanoparticles is determined by applying the radius percentage difference (R$_p$) as predicted by Shivakumara [53]:

$$R_p = \frac{R_h(CN) - R_d(CN)}{R_h(CN)} \text{ x } 100\% \tag{1}$$

where *CN* is the coordination number, $R_h(CN)$ is the ionic radius of the host cation, and $R_d(CN)$ is the ionic radius of the dopant ion. For efficacious doping, the radius percentage difference between the host ion and the dopant ion must be less than 30% [54]. The R_p between Na ion (CN = 12, R$_{Na}$ = 1.39 Å) and Sr (CN = 12, R$_{Sr}$ = 1.44 Å) is 3%. Similarly, the R_p of Na (CN = 6, R$_{Na}$ = 1.02 Å) and Zr (CN = 6, R$_{Zr}$ = 0.72 Å) is 42%. Therefore, Na will preferentially occupy the Sr site since the radius percentage difference of 3% is far below the threshold value of 30%. The incorporation of Na at the Sr site is affirmed by the shift of (200) diffraction peak to higher angles for all Sr$_{1-x}$Na$_{2x}$ZrO$_3$ samples vis-a-vis

the SrZrO$_3$ sample (see Fig. 2B).

Another effect of incorporating Na $^+$ at Sr^{2+} site is the Goldschmidt's tolerance factor T, which determines the stability of the perovskite. Knowing the tolerance factor can provide a meaningful probabilistic approximation for a given compound as a stable perovskite [54]. The Goldschmidt's tolerance factor is also dependent on the relative ionic radii of A-site cation, (rA), B-site cation (r$_B$), and the oxygen anion (rO) in an ABO$_3$ perovskite structural configuration, expressed as [49];

$$t = \frac{\langle r_A \rangle + r_O}{\sqrt{2}(r_B + r_O)} \tag{2}$$

where, $\langle r_A \rangle$ is the average radius of Sr and Na in Sr$_{1-x}$Na$_{2x}$ZrO$_3$ perovskite nanocrystal. In an idealistic cubic perovskite, the tolerance factor is unity, but stable perovskite with non-cubic symmetry occurs when the tolerance factor deviates from unity [55]. The calculated values of tolerance factors for different Na concentrations are shown in Table 2. The result shows the tolerance factor values of Sr$_{1-x}$Na$_{2x}$ZrO$_3$ perovskites range from 0.95 to 1.12 for Na concentrations $0 \leq x \geq 0.4$. The addition of Na at $x = 0.1$ yields a tolerance factor value close to 1 (0.99), which is superior to the undoped perovskite with a tolerance factor value of 0.95, indicating a more stable perovskite structure. However, at $x \geq 0.2$, the tolerance factor is > 1. Other reports also have t values > 1, though without explanations on the implication [56–58]. Kim and Yu reported an increasing trend of tolerance factor values from 1.013 to 1.030 and concluded that cubic perovskite maintains a tolerance factor of 1 ± 0.05. In this work, the tolerance factor also showed an increasing trend with values above the limit suggested by Kim and Yun. We interpret the $t > 1$ values obtained in this work as a result of the presence of a weak ZrO$_2$ second phase. The presence of the ZrO$_2$ layer for Na-doped samples suggests that some Na might have occupied Zr sites in the octahedron. This will lead to the displacement of Zr ions which then combine with surface oxygen to form the ZrO$_2$ layer. Increasing the concentration of Na means that more Zr will be displaced from the octahedron and thus more ZrO$_2$ with enhanced XRD peak intensity.

The Jahn-Teller (JT) distortion parameter was obtained from Rietveld analysis as a function of Zr concentration where the coherent JT distortion reduces (i.e., the spacing between Zr and O bonds). Therefore, the ZrO$_6$ octahedral distortion tends to decrease, thus, the Na actively prevents the greater distortion of the perovskite structure. The result is consistent with the observation from Goldschmidt's tolerance factor. The coherent JT distortion is determined using the JT parameter [59] expressed in equation (3). Here, a drastic increase of the JT distortion (σ_{JT}) parameter was observed at the initial doping (σ_{JT} = 3.1), considering the undoped sample as the standard state of the perovskite.

$$\sigma_{JT} = \sqrt{\frac{1}{3}\Sigma_i\left[(Zr - O)_i - \langle Zr - O \rangle\right]^2} \tag{3}$$

Furthermore, the geometrical parameters of the *JT* effect also can be obtained through the coordination number, and from the three-bond length: long (*l*), short (*s*), and medium (*m*) of (*Zr–O*) [60,61]. The distortion parameter (Δ) for the BO$_6$ octahedron is given by:
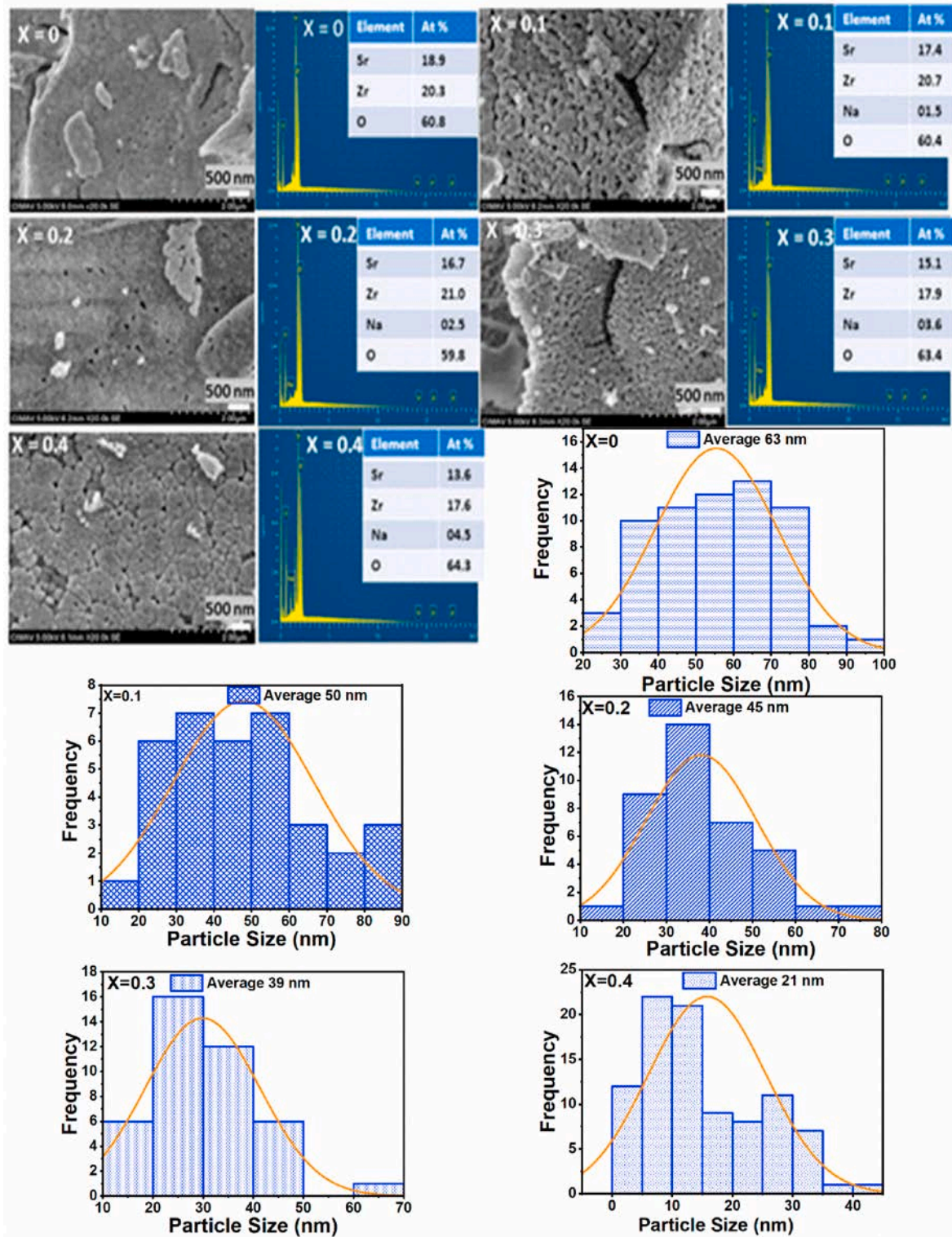
Fig. 3. SEM images and EDX spectra of $Sr_{1-x}Na_{2x}ZrO_3$ perovskite; Particle size distribution histogram of $Sr_{1-x}Na_{2x}ZrO_3$ perovskite.

$$\Delta = \frac{1}{Z}\sum_{n=1,Z}\left\{\frac{d_n - \langle d\rangle}{\langle d\rangle}\right\}^2 \tag{4}$$

where Z is the coordination number, d is the bond length, and $\langle d\rangle$ is the average bond length. The Δ of ZrO_6 octahedra determined for the five compositions are consistent with the σ_{JT} parameter, and decreases with the increasing of the quantity of Na^+ doping. The values of Δ

$(Zr - O) \times 10^{-4}$ are 9.55, 21.32, 5.10, 3.79, and 2.50 for $x = 0$, 0.1, 0.2, 0.3, and 0.4, respectively. Another way to know the degree of deformation is by the inclination of the ZrO_6 octahedron around the [111] crystallographic direction [60], the angle of which has been obtained from Equations (5) and (6).

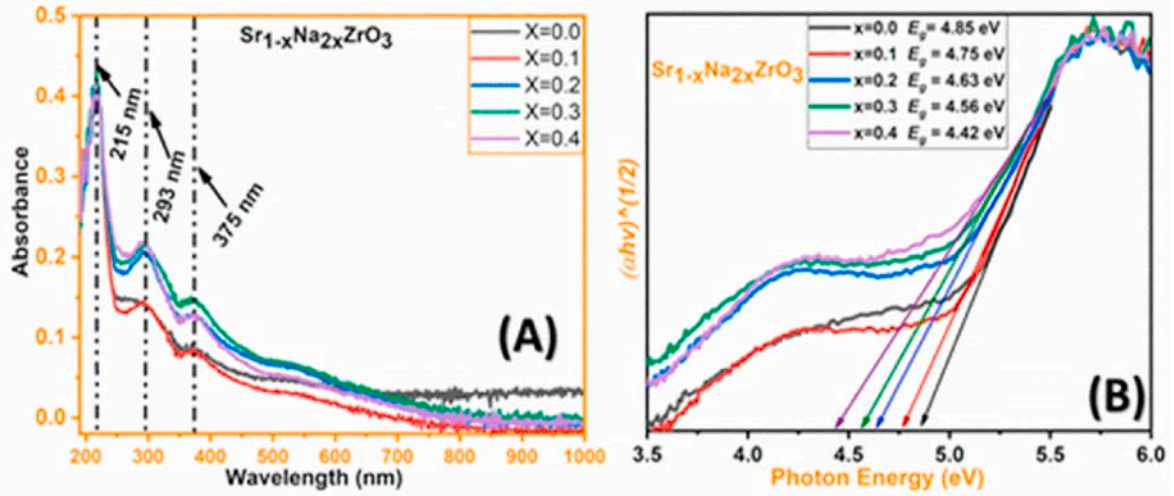$$cos\,\theta_1 = \frac{2 - 5\,cos^2\varphi_1}{2 + cos^2\varphi_1} \tag{5}$$

Fig. 4. UV–vis absorbance spectra: (A) Optical Absorbance, (B) Band gap energy of $Sr_{1-x}Na_{2x}ZrO_3$ perovskite nanoparticles.

$$cos\,\theta_2 = \frac{1 - 4\,cos^2\varphi_2}{3} \qquad (6)$$

where θ_1 and θ_2 are the Zr–O–Zr bond angles of the octahedron. The calculated mean tilt angles of ZrO_6 octahedra around the quasi-cubic [111] direction are $13.61, 13.69, 13.72, 13.97,$ and 14.96 for $x = 0, 0.1, 0.2, 0.3,$ and 0.4, respectively. These values suggest that the tilt angle of ZrO_6 octahedra along the [111] direction increases with increasing Na^+ concentrations in the solid solution, indicating a decreasing trend in lattice distortion. Everything discussed earlier is consistent with the claim that sodium ion plays an active role in preventing large deformations in perovskites structure. This behaviour is attributed to the vacancy defect caused by the A-site stabilizing charge.

Whenever Sr ions are partly replaced by Na ions, defects such as oxygen vacancies ($V_O^{\bullet\bullet}$) are formed in the crystal lattice according to equation (7),

$$Zr_2O \xrightarrow{2SrO} 2Zr'_{Sr} + O_O^x + V_O^{\bullet\bullet} \qquad (7)$$

The equilibrium defects at the annealing temperature of the perovskite according to the Kröger-Vink-Notation is expressed in equation (8) which can be interpreted in terms of the creation of $Zr^{4+} - V_O^{\bullet\bullet} - Zr^{4+}$ clusters.

$$2Zr_{zr}^x + O_O^x \leftrightarrow 2Zr'_{Sr} + V_O^{\bullet\bullet} + \frac{1}{2}O_2(g) \qquad (8)$$

After this lattice stabilization, any increase in Na ion in the solid solution leads to a decrease in the *JT* distortion parameter. The average Zr–O–Zr bond angle has the same trend.

The average crystallite size of each sample was estimated by averaging the crystallite sizes obtained from the most prominent and symmetric peaks of the corresponding diffraction pattern using Debye Scherrer's equation:

$$D = 0.9\lambda / \beta \cos\theta \qquad (9)$$

where D is the crystallite size, λ is the wavelength of X-ray, θ is the Bragg's angle, and β is the FWHM (Full width at half maximum). The calculated values of average crystallite sizes are presented in Table 2 and show decreasing trend with increasing Na ion concentration. This result is in agreement with the declining trend already report for the XRD peak intensity as well as the peak broadening as a function of Na^+ concentrations.

3.3. Scanning electron microscopy (SEM) analysis

Fig. 3 shows the morphologies of $Sr_{1-x}Na_{2x}ZrO_3$ perovskite nanoparticles at different compositions ($x = 0, 0.1, 0.2, 0.3,$ and 0.4). From the image, the particles of pure $SrZrO_3$ compound are spherical shape with a high degree of agglomeration. The Na incorporated samples show some spherical voids/pores which formed from the escaping gas during the annealing process. The measured particle sizes of $Sr_{1-x}Na_{2x}ZrO_3$ perovskite 63 nm, 50 nm, 45 nm, 39 nm, and 29 nm for $x = 0, 0.1, 0.2, 0.3,$ and 0.4 Na^+ concentrations, respectively. The histograms displaying particle size distribution in each sample are presented in Fig. 3. There's a decrease in particle size with increasing Na ion concentration following the same trend as the estimated average crystallite sizes obtained from the XRD analysis.

EDX analysis of pure $SrZrO_3$ samples confirmed the presence of Sr, Zr, and O. In addition to the listed elements, the $Sr_{1-x}Na_{2x}ZrO_3$ samples also confirmed the presence of Na, as shown in Fig. 3. EDX results show that the stoichiometric compositions of the various elements (Sr, Zr, Na, and O) at atomic percentages are close to the theoretical values. The atomic ratio of Sr:Zr and (Sr + Na): Zr for undoped and low Na doping concentrations ($x \leq 1$) is ≈ 0.9, and ≈ 1 for higher Na concentrations ($x \geq 1$). From the EDX table, (Fig. 3 inset), the atomic percent for Zr after Na doping at $x = 0.1$ *to* $x = 0.2$ to has the same value as for the undoped sample ($\approx 20\%$), demonstrating that Na was marginally doped at Zr sites in $Sr_{1-x}Na_{2x}ZrO_3$. However, the atomic percent of Zr reduced to 17.9/17.6% for Na doping at $x = 0.3$ to $x = 0.4$ concentrations suggesting a partial substitution of Zr by Na. Moreover, for all doping concentrations ($x = 0.1$ *to* 0.4), the atomic percentage of Sr decreases monotonically with the systematic increase of Na ion concentration, indicating that Na^+ preferentially replaces Sr^{2+} at its site. This result is in agreement with the XRD result.

3.4. Ultraviolet–visible absorption spectroscopy analysis

The optical properties of Na-doped $SrZrO_3$ nanoparticles were investigated with the help of diffuse reflectance spectroscopy. All spectra were recorded at room temperature over a wavelength range of 200–1000 nm, as shown in Fig. 4A. All samples show three absorption bands at 215 *nm*, 293 *nm*, and 375 *nm*. For Na doped samples, the intensities of these bands are enhanced and become apparent. Wood and Tauc's expression in equation (10) [62,63] gives the relationship between optical energy band gap, absorption coefficient, and photon energy:

$$\alpha h v \, \alpha \, (h v - E_g)^m \qquad (10)$$

Table 3
Band Gap energy of $Sr_{1-x}Na_{2x}ZrO_3$ perovskite nanoparticles.

Sodium Concentration (X)	Sample Type	Band gap (eV)
0	$SrZrO_3$	4.85
0.1	$Sr_{0.9}Na_{0.2}ZrO_3$	4.75
0.2	$Sr_{0.8}Na_{0.4}ZrO_3$	4.63
0.3	$Sr_{0.7}Na_{0.6}ZrO_3$	4.56
0.4	$Sr_{0.6}Na_{0.8}ZrO_3$	4.42

Fig. 5. FTIR spectrum of $Sr_{1-x}Na_{2x}ZrO_3$ perovskite nanoparticles.
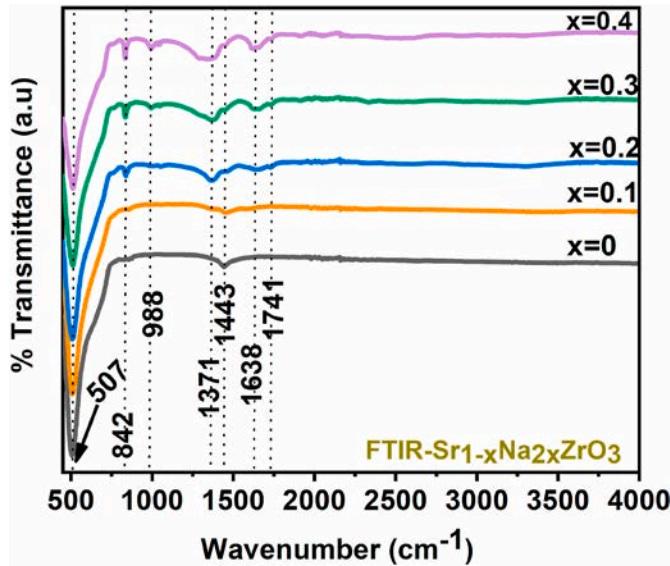
Fig. 6. Raman spectra of $Sr_{1-x}Na_{2x}ZrO_3$ perovskite nanoparticles.

where E_g is the optical band gap, α is the linear absorption coefficient of the sample, h the Planck's constant, ν is the frequency, $h\nu$ is the photon energy, and m is a constant depending on the nature of transition, $m = 1/2$, 3/2, 2 or 3 for direct allowed, direct forbidden, indirect allowed, or indirect forbidden transition, respectively. The value of the exponent "$m = 2$" was taken in this analysis because studies have shown that pure strontium zirconate has a light absorption process governed by indirect electronic transitions [64,65]. However, it has been shown that the indirect transition for pure $SrZrO_3$ transforms to direct transition for doped $SrZrO_3$ perovskites [23,66–68].

The energy diagram of $(\alpha h\nu)^{1/2}$ versus $h\nu$ is shown in Fig. 4B. The optical band gap is obtained from the graph by extrapolating the linear portion of each spectrum to the value of $(\alpha h\nu)^{1/2} = 0$ on the energy axis. The obtained energy band gap values are presented in Table 3. With increasing Na^+ concentrations, the energy band gap values show a downward trend. Sedeek [43] reported a similar energy band gap narrowing trend in La-doped $SrZrO_3$.

The reduction in the energy band gap (E_{gap}) is attributed to several factors [69–71]; (i) lattice disorder; increasing lattice defects by Na doping will introduce localized states within the energy band gap region [62]. Furthermore, the replacement of Zr atoms by Na in the octahedron allows the formation of intermediate energy levels in the bandgap energy region, resulting in additional energy levels in the bandgap of disordered Na-doped $SrZrO_3$ perovskites [71]; (ii) generation of oxygen vacancies as a result of substituting a high valence ion (Sr^{2+} or Zr^{4+}) with a low valence ion (Na^+) would promote the formation of localized states in the band gap [42,43]. The density of localized states will increase with the impurity concentration, thereby narrowing the energy bandgap. (iii) The third factor is the grain size effect or quantum confinement effect; according to the effective mass approximation, the energy band gap is inversely proportional to the grain size. Thus, an increase in the grain size should lead to a decrease in the energy band
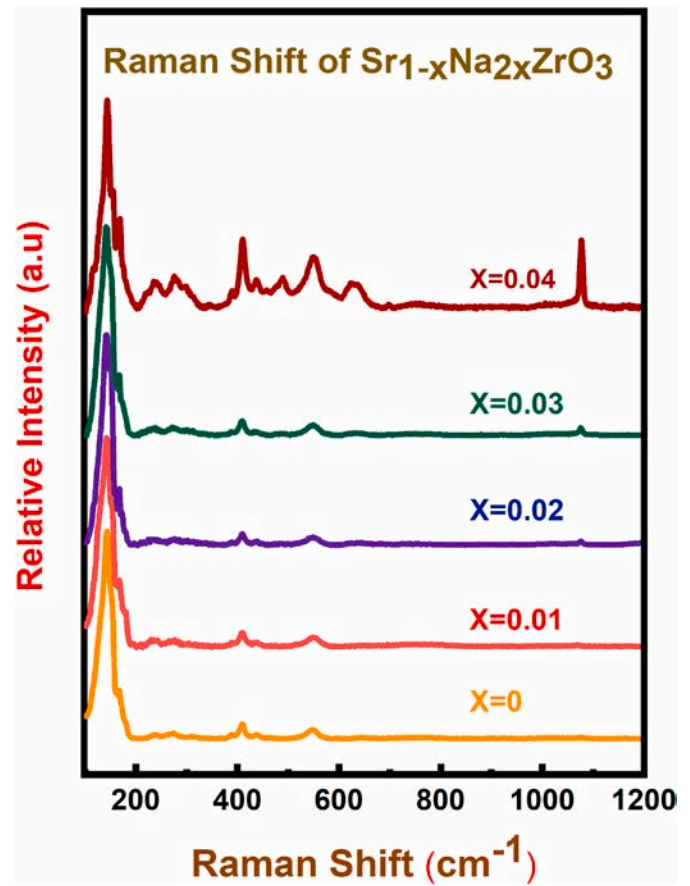
gap, however, this is not the case from the optical results in Table 3, suggesting that the quantum effect has no role in narrowing the energy band gap for our samples. Moreover, the decline in energy band gap is consistent with increase in lattice distortion with high Na^+ concentration as already observed from the XRD result.

3.5. FTIR analysis

The absorption and band position of FTIR spectra depends on so many factors such as the chemical composition, crystal structure, strain, and sample morphology. Fig. 5 depicts the FTIR spectrum of $Sr_{1-x}Na_{2x}ZrO_3$ perovskite in the wavenumber range 400 cm^{-1} to 4000 cm^{-1}. Infrared (IR) spectrums below 1000 cm^{-1} are attributable to the Zr–O bonds deformation mode in ZrO_6 octahedra or Zr–O–Zr bridge deformation. Associated with Zr–O molecular vibrations is the band between 400 cm^{-1} and 910 cm^{-1}.

The irreducible representation of the orthorhombic *Pbnm* phase of $SrZrO_3$ Γ has 25 infrared activation modes at the Γ point, $9B_{1u}$, $7B_{2u}$, and $9B_{3u}$, respectively. Seven major bands of these patterns were observed in this analysis. The spectra of undoped ($SrZrO_3$) and $Sr_{0.9}Na_{0.2}ZrO_3$ show absorption only around 507 cm^{-1} and 1443 cm^{-1}. The activated stretching vibration mode of the Zr–O band at 507 cm^{-1} is the result of antisymmetric stretching vibration of the ZrO_6 octahedron [72]. The band at 842 cm-1 and 988 cm-1 are related to the bending mode of Na–O [[39,73]]; while bands at 1371 cm-1 and 1443 cm-1 could be related to the stretching vibration of nitrate radical group (NO3) [[39,73,74]]. The vibration peak observed at 1638 cm-1 and 1741 cm-1 are attributed to symmetrical stretching of Sr–O bonds.
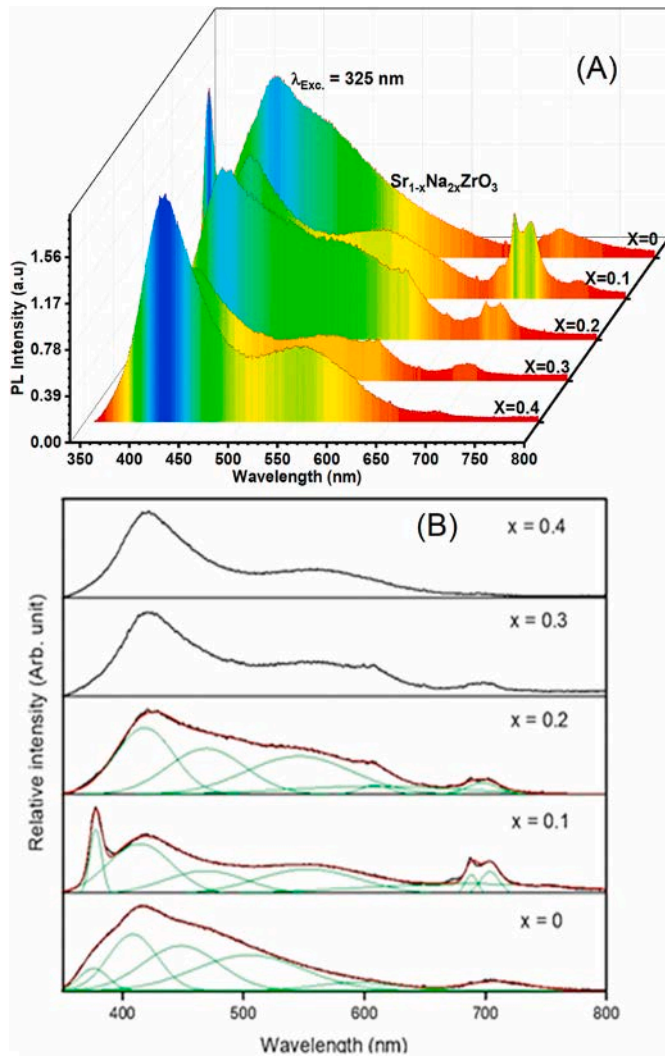
Fig. 7. Photoluminescence emission spectra of $Sr_{1-x}Na_{2x}ZrO_3$ nanocrystals (x = 0, 0.1, 0.2, 0.3, and 0.4) (A). The green curves indicate the deconvoluted bands (B).

3.6. Raman spectra analysis

Raman spectroscopy is employed to determine the relationship between the lattice vibrational modes and the resonant patterns. Fig. 6 shows the Raman phonon frequencies of the $Sr_{1-x}Na_{2x}ZrO_3$ perovskite in the frequency range 100–1200 cm−1 $SrZrO_3$ has 24 Raman activity modes described by $7A_g$, $5B_{1g}$, $7B_{2g}$, and $5B_{3g}$ [75]. However, only 12 Raman modes are observed for $Sr_{1-x}Na_{2x}ZrO_3$, $5A_g$ (106.8, 169.4, 242.8, 413.3, 553.3 cm^{-1}), $5B_{g2}$ (117.1, 143.9, 281.3, 392.7, 442.4 cm^{-1}), $1B_{g3}$ (701.1 cm^{-1}) in the sampled spectra region shown in Fig. 6. The low polarizabilities of some modes and small distortions in the ideal $SrZrO_3$ perovskite structure, which reduces spectral resolution are the reasons the other 12 active modes were not observed for these samples [50, 76–82]. All observed peaks are oriented to the $SrZrO_3$ orthorhombic characteristics and are consistent with the XRD results.

The lowest frequency vibrator range of 100 cm^{-1} to 200 cm^{-1} is attributed to the lattice vibrations of the Sr ions in the A site with ZrO_6 octahedron [64,78,80]. In the range from 200 cm^{-1} to 400 cm^{-1}, the vibrational bands are associated with O^{2-}, while the modes at 242.8 cm^{-1}, 281.3 cm^{-1}, and 347.7 cm^{-1} are associated with Sr^{2+} ions. Vibration frequency modes above 400 cm^{-1} to 600 cm^{-1} are largely attributed to Zr–O bonds. Meanwhile, the frequency modes at 392.7, 413.3, 442.4 and 489.1 cm^{-1} are assigned to the bending vibrations of

Zr–O bond. Finally, the frequency observed at 553.3 cm^{-1} is the result of Zr–O stretching vibrations.

In the observed spectra, bands at 152.9; 300.4; 347.7; 489.1; 628.7; 701.1 cm^{-1} (particularly for Na doping at $x = 0.4$) are typical for monoclinic zirconia [83,84]. A critical look at the Raman spectra in Fig. 6 and broadband deconvolution of the 100–200 cm^{-1} region shows the persistence of the 152.9 cm^{-1} bands in all Na-doped samples, albeit with different intensities. This fact is an indication that the monoclinic phase is present in all doped samples. This result confirms the presence of the monoclinic phase in the XRD patterns. A very strong narrow band at 1077.5 cm^{-1} indicates the presence of surface $NaNO_3$ species [85].

A very important parameter that can be extracted from the Raman spectra is the effective phonon energy (E_{ph}) of the $Sr_{1-x}Na_{2x}ZrO_3$ nanocrystals. The E_{ph} defines the rate of radiationless transition in a material [86]. The effective phonon energy of $Sr_{1-x}Na_{2x}ZrO_3$ was determine from the expression [87]:

$$E_{ph} = \frac{\sum_i E_i w_i A_i}{\sum_i w_i A_i} \qquad \qquad 11$$

where E_i, w_i, and A_i are the position, FWHM, and relative intensity of each Lorentzian sub-band, respectively. The values of E_i, w_i, and A_i were obtained by Lorentzian fitting of the spectrum. From equation (10), the calculated value of phonon energy for $Sr_{1-x}Na_{2x}ZrO_3$ nanocrystals is 442 cm^{-1}. Low phonon energy decreases the probability of nonradiative multiphonon relaxation of excited activator ions throughout the vibrational bands of the host lattice [87]. Therefore, the low phonon energy of $Sr_{1-x}Na_{2x}ZrO_3$ nanocrystal makes it a promising candidate for photonic applications.

3.7. Photoluminescence properties of $Sr_{1-x}Na_{2x}ZrO_3$ perovskite

The photoluminescence emission (PL) spectra for $Sr_{1-x}Na_{2x}ZrO_3$ (x = 0, 0.1, 0.2, 0.3 and 0.4) perovskite nanocrystals obtained by excitation with He–Cd laser of wavelength 325 nm are presented in Fig. 7A and (B) (deconvoluted bands). The excitation wavelength of 325 nm is below the energy band gap for all samples and therefore only able to excite electrons within the band gap of the $SrZrO_3$ structure. The pure and ordered $SrZrO_3$ structure does not luminescence thus, the broad PL spectra in Fig. 7 covering 300–800 nm range is often attributed to a distorted $SrZrO_3$ structure and the presence of localized energy states in the band gap [88,89]. Both the undoped (pure) and Na-doped samples spectra were deconvoluted into six components using Gaussian fitting as shown for x = 0, 0.1, and 0.2 samples namely: 376–418 nm (violet), 448–469 nm (blue), 504–553 (green), 594–608 nm (orange), and 688–709 nm (red). The existence of these multicolour emission bands is an indication of different categories of electronic transition paths in the band gap, each associated with specific structural arrangement or defect. The common defects in disordered $SrZrO_3$ are the shallow and deep defects generated by Zr–O and Sr–O complex clusters in the band gap [43]. The violet and blue emission bands are ascribed to shallow defects and complex oxygen-deficient cluster vacancies, respectively in the band-gap. These shallow defects gradually disappeared with increasing order/stability in the lattice. Fig. 7 also shows the narrow intense violet peak at 376 nm drastically reduced in intensity (the 408 nm peak shift to higher wavelength) at Na$^+$ incorporation ($x = 0.1$) and disappeared completely at higher Na$^+$ concentrations where the tolerance factor (from XRD) indicated a more stabilized structure. The green, orange, and red emissions are associated with defects deeply inserted in the band gap and to an increased disorder in the lattice. With the incorporation of Na$^+$ in the lattice, the green emission band is enhanced (blue emission decreased) and becomes more distinct at higher dopant concentrations due to increased disorder in the $SrZrO_3$ crystal lattice. Both XRD and energy band gap results indicated an increased disorder at higher Na$^+$ doping concentrations. The red emission line at about 688–709 nm is
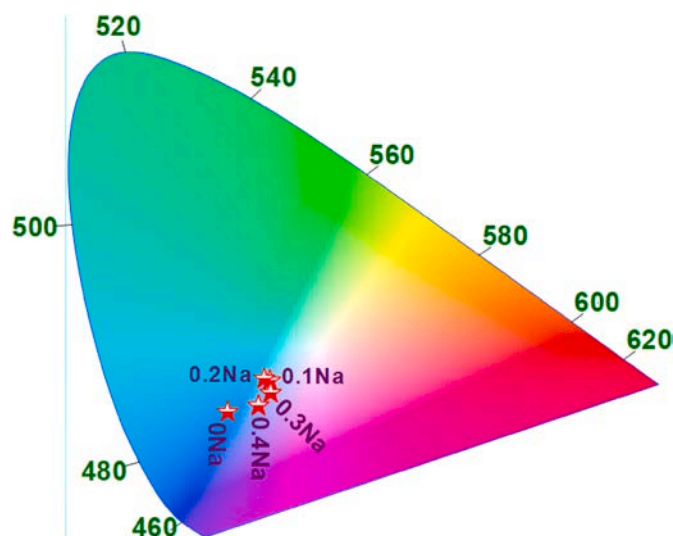
Fig. 8. CIE diagram of $Sr_{1-x}Na_{2x}ZrO_3$ nanocrystals ($x = 0$, 0.1, 0.2, 0.3, and 0.4).

known to often accompany high temperature treatment of $SrZrO_3$ perovskite above 800 °C [90]. The mechanism responsible for the formation of this red emission line is not well studied or known, but a few reports have ascribed it to F-centers formed by cation centers [91] as well as high crystallinity of $SrZrO_3$ (Lee et al., 2011) [90]. The red line is strongest for $Sr_{0.9}Na_{0.2}ZrO_3$ (or $x = 0.1$) sample where the structural stability is ideal and then decreases monotonously at higher Na^+ concentrations (Fig. 7). Thus, it is clear that Na^+ incorporation in the lattice increases more the effect of the deep defect states.

Commission International de I' Eclairage (CIE) 1931 x-y chromaticity diagram of $Sr_{1-x}Na_{2x}ZrO_3$ are shown in Fig. 8. The corresponding chromaticity coordinates are (0.2007, 0.2180), (0.2531, 0.2720), (0.2459, 0.2752), (0.2541, 0.2508) and (0.2388, 0.2290) for $x = 0$, 0.1, 0.2, 0.3 and 0.4 of Na, respectively. From the spectra, the coordinates of the energized samples shift from the blue to the white region when the Na concentration increases $x = 0.1$ to $x = 0.2$ i.e., when the red emission band is strong, and reverted to blue light at higher Na^+ concentrations ($x > 0.2$) [92,93]. Thus, $Sr_{1-x}Na_{2x}ZrO_3$ perovskite as a promising phosphor for blue and white light applications.

4. Conclusion

In summary, nanoparticles $Sr_{1-x}Na_{2x}ZrO_3$ ($0 \le x \le 0.4$) perovskite were synthesized by a simplified sol–gel route using citrate-ethylene glycol as the chelating agent. TGA-DSC analysis shows that Na influences the faster decomposition process of $Sr_{1-x}Na_{2x}ZrO_3$ structure. X-ray diffraction and Rietveld refinement showed that these compositions crystallized in an orthorhombic phase with the Pbnm space group. The four distinct Raman bands (A_g, B_{1g}, B_{2g}, B_{3g}) confirm the orthorhombic phase and are consistent with Goldschmidt's tolerance factor. The incorporation of Na into the $SrZrO_3$ lattice enhances the stability of the orthorhombic perovskite. The Jahn-Teller (σJT) distortion parameter verifies that Na play an active role in preventing the large distortion of the perovskite structure. The estimated crystallite size from XRD analysis decreased with increasing Na incorporation to 19 nm. The band gap narrowing from 4.85 eV to 4.42 eV is attributed to localized states in the energy bandgap due to lattice distortion and oxygen vacancies. Thus, high optical transparency and stable structural stability could make $Sr_{1-x}Na_{2x}ZrO_3$ perovskite nanocrystal a promising phosphor matrix for display and lighting applications when transition element or rare-earth activators are incorporated.

References

[1] IEA. Global Energy Review. https://www.iea.org/reports/global-energy-review-2021.

[2] S.D. Stranks, G.E. Eperon, G. Grancini, et al., Electron-hole diffusion lengths exceeding 1 micrometer in an organometal trihalide perovskite absorber, 1979, Science 342 (6156) (2013) 341–344, https://doi.org/10.1126/science.1243982.

[3] Y. Kanemitsu, T. Handa, Photophysics of metal halide perovskites: from materials to devices, Jpn. J. Appl. Phys. 57 (9) (2018), 090101, https://doi.org/10.7567/JJAP.57.090101.

[4] D. Shi, V. Adinolfi, R. Comin, et al., Low trap-state density and long carrier diffusion in organolead trihalide perovskite single crystals, 1979, Science 347 (6221) (2015) 519–522, https://doi.org/10.1126/science.aaa2725.

[5] H.Y. Kim, J. Shin, I.C. Jang, Y.W. Ju, Hydrothermal synthesis of three-dimensional perovskite NiMnO3 oxide and application in supercapacitor electrode, Energies 13 (1) (2019) 36, https://doi.org/10.3390/en13010036.

[6] J. Shen, X. Zhang, S. Das, E. Kioupakis, C.G. van de Walle, Unexpectedly strong auger recombination in halide perovskites, Adv. Energy Mater. 8 (30) (2018), 1801027, https://doi.org/10.1002/aenm.201801027.

[7] X. Zhang, M.E. Turiansky, C.G. van de Walle, All-inorganic halide perovskites as candidates for efficient solar cells, Cell Rep Phys Sci 2 (10) (2021), 100604, https://doi.org/10.1016/j.xcrp.2021.100604.

[8] S.A. Veldhuis, P.P. Boix, N. Yantara, et al., Perovskite materials for light-emitting diodes and lasers, Adv. Mater. 28 (32) (2016) 6804–6834, https://doi.org/10.1002/adma.201600669.

[9] Z.K. Tan, R.S. Moghaddam, M.L. Lai, et al., Bright light-emitting diodes based on organometal halide perovskite, Nat. Nanotechnol. 9 (9) (2014) 687–692, https://doi.org/10.1038/nnano.2014.149.

[10] G. Cheng, Y. Liu, T. Chen, et al., Efficient all-inorganic perovskite light-emitting diodes with improved operation stability, ACS Appl. Mater. Interfaces 12 (15) (2020) 18084–18090, https://doi.org/10.1021/acsami.9b23170.

[11] Q. Wang, X. Wang, Z. Yang, et al., Efficient sky-blue perovskite light-emitting diodes via photoluminescence enhancement, Nat. Commun. 10 (1) (2019) 5633, https://doi.org/10.1038/s41467-019-13580-w.

[12] L. Gu, K. Wen, Q. Peng, W. Huang, J. Wang, Surface-Plasmon-enhanced perovskite light-emitting diodes, Small 16 (30) (2020), 2001861, https://doi.org/10.1002/smll.202001861.

[13] W.S. Yang, J.H. Noh, N.J. Jeon, et al., High-performance photovoltaic perovskite layers fabricated through intramolecular exchange, 1979, Science 348 (6240) (2015) 1234–1237, https://doi.org/10.1126/science.aaa9272.

[14] M. Liu, M.B. Johnston, H.J. Snaith, Efficient planar heterojunction perovskite solar cells by vapour deposition, Nature 501 (7467) (2013) 395–398, https://doi.org/10.1038/nature12509.

[15] T.S. Kao, K.B. Hong, Y.H. Chou, J.F. Huang, F.C. Chen, T.C. Lu, Localized surface plasmon for enhanced lasing performance in solution-processed perovskites, Opt Express 24 (18) (2016), 20696, https://doi.org/10.1364/OE.24.020696.

[16] C. Zhou, J. Yu, H. Dong, et al., Broad-band lead halide perovskite quantum dot single-mode lasers, J Mater Chem C Mater 8 (39) (2020) 13642–13647, https://doi.org/10.1039/D0TC02551H.

[17] D. Liu, B.B. Yu, M. Liao, et al., Self-powered and broadband lead-free inorganic perovskite photodetector with high stability, ACS Appl. Mater. Interfaces 12 (27) (2020) 30530–30537, https://doi.org/10.1021/acsami.0c05636.

[18] J. Huang, Y. Yuan, Y. Shao, Y. Yan, Understanding the physical properties of hybrid perovskites for photovoltaic applications, Nat. Rev. Mater. 2 (7) (2017), 17042, https://doi.org/10.1038/natrevmats.2017.42.

[19] S.A. Kulkarni, T. Baikie, P.P. Boix, N. Yantara, N. Mathews, S. Mhaisalkar, Band-gap tuning of lead halide perovskites using a sequential deposition process, J. Mater. Chem. 2 (24) (2014) 9221–9225, https://doi.org/10.1039/C4TA00435C.

[20] S. Hou, M.K. Gangishetty, Q. Quan, D.N. Congreve, Efficient blue and white perovskite light-emitting diodes via manganese doping, Joule 2 (11) (2018) 2421–2433, https://doi.org/10.1016/j.joule.2018.08.005.

[21] M. Kato, T. Fujiseki, T. Miyadera, et al., Universal rules for visible-light absorption in hybrid perovskite materials, J. Appl. Phys. 121 (11) (2017), 115501, https://doi.org/10.1063/1.4978071.

[22] L. Protesescu, S. Yakunin, M.I. Bodnarchuk, et al., Nanocrystals of cesium lead halide perovskites (CsPbX $_3$, X = Cl, Br, and I): novel optoelectronic materials showing bright emission with wide color gamut, Nano Lett. 15 (6) (2015) 3692–3696, https://doi.org/10.1021/nl5048779.

[23] S.S.A. Gillani, R. Ahmad, M. Rizwan, et al., Effect of magnesium doping on band gap and optical properties of SrZrO3 perovskite: a first-principles study, Optik 191 (2019) 132–138, https://doi.org/10.1016/j.ijleo.2019.05.099.

[24] E. Li, W. Ma, P. Zhang, et al., The effect of Al3+ doping on the infrared radiation and thermophysical properties of SrZrO3 perovskites as potential low thermal infrared material, Acta Mater. 209 (2021), 116795, https://doi.org/10.1016/j.actamat.2021.116795.

[25] R.D. Shannon, Revised effective ionic radii and systematic studies of interatomic distances in halides and chalcogenides, Acta Crystallogr. A 32 (5) (1976) 751–767, https://doi.org/10.1107/S0567739476001551.

[26] X. Mao, Y. Bai, J. Yu, B. Ding, Insights into the flexibility of ZrM $_x$ O $_y$ (M = Na, Mg, Al) nanofibrous membranes as promising infrared stealth materials, Dalton Trans. 45 (15) (2016) 6660–6666, https://doi.org/10.1039/C6DT00319B.

[27] K. Hilpert, D. Das, M. Miller, D.H. Peck, R. Weiß, Chromium vapor species over solid oxide fuel cell interconnect materials and their potential for degradation processes, J. Electrochem. Soc. 143 (11) (1996) 3642–3647, https://doi.org/10.1149/1.1837264.

[28] Q. Tian, L. Zhang, J. Liu, et al., Synthesis of MoS $_2$/SrZrO $_3$ heterostructures and their photocatalytic H $_2$ evolution under UV irradiation, RSC Adv. 5 (1) (2015) 734–739, https://doi.org/10.1039/C4RA11135D.

[29] R. Vali, Band structure and dielectric properties of orthorhombic SrZrO3, Solid State Commun. 145 (9–10) (2008) 497–501, https://doi.org/10.1016/j.ssc.2007.12.009.

[30] S.K. Gupta, P.S. Ghosh, N. Pathak, A. Arya, V. Natarajan, Understanding the local environment of Sm $^{3+}$ in doped SrZrO $_3$ and energy transfer mechanism using time-resolved luminescence: a combined theoretical and experimental approach, RSC Adv. 4 (55) (2014) 29202–29215, https://doi.org/10.1039/C4RA04262J.

[31] R. Watanabe, Y. Saito, C. Fukuhara, Dehydrogenation of ethylbenzene over zirconium-based perovskite-type catalysts of AZrO3 (A: Ca, Sr, Ba), Appl. Catal. Gen. 482 (2014) 344–351, https://doi.org/10.1016/j.apcata.2014.06.012.

[32] S. Hossain, A.M. Abdalla, S.N.B. Jamain, J.H. Zaini, A.K. Azad, A review on proton conducting electrolytes for clean energy and intermediate temperature-solid oxide fuel cells, Renew. Sustain. Energy Rev. 79 (2017) 750–764, https://doi.org/10.1016/j.rser.2017.05.147.

[33] JR. de O. Lima, Y.A. Ghani, R.B. da Silva, et al., Strontium zirconate heterogeneous catalyst for biodiesel production: synthesis, characterization and catalytic activity evaluation, Appl. Catal. Gen. 445–446 (2012) 76–82, https://doi.org/10.1016/j.apcata.2012.08.005.

[34] M. Venugopal, H.P. Kumar, R. Jayakrishnan, Synthesis, characterization and photoluminescent properties of Sm3+/Dy3+ doped strontium zirconate perovskites, J. Electroceram. 44 (3–4) (2020) 163–172, https://doi.org/10.1007/s10832-020-00207-6.

[35] Taxak VB. Sheetal, R. Arora, Khatkar SP. Dayawati, Synthesis, structural and optical properties of SrZrO3:Eu3+ phosphor, Rare Earths 32 (4) (2014) 293–297, https://doi.org/10.1016/S1002-0721(14)60070-3.

[36] A. Zhang, M. Lü, G. Zhou, Y. Zhou, Z. Qiu, Q. Ma, Synthesis, characterization and luminescence of Eu3+-doped SrZrO3 nanocrystals, J. Alloys Compd. 468 (1–2) (2009) L17–L20, https://doi.org/10.1016/j.jallcom.2008.01.030.

[37] J. Huang, L. Zhou, Z. Wang, et al., Photoluminescence properties of SrZrO3:Eu3+ and BaZrO3:Eu3+ phosphors with perovskite structure, J. Alloys Compd. 487 (1–2) (2009) L5–L7, https://doi.org/10.1016/j.jallcom.2009.07.153.

[38] C. Wang, J. Wang, M. Yuan, et al., The structure and electronic properties of Ge/SrZrO 3, Vacuum 130 (2016) 165–173, https://doi.org/10.1016/j.vacuum.2016.05.015.

[39] N. Singh, I.W. Kim, S. Watanabe, T.K. Gundu Rao, V. Singh, Trivalent gadolinium doped SrZrO3 perovskite ceramic: sol-gel synthesis, paramagnetic centres, and luminescence studies, Ceram. Int. 46 (14) (2020) 22108–22115, https://doi.org/10.1016/j.ceramint.2020.05.261.

[40] W. Zając, D. Rusinek, K. Zheng, J. Molenda, Applicability of Gd-doped BaZrO3, SrZrO3, BaCeO3 and SrCeO3 proton conducting perovskites as electrolytes for solid oxide fuel cells, Open Chem 11 (4) (2013) 471–484, https://doi.org/10.2478/s11532-012-0144-9.

[41] D.J. Lee, D.H. Kim, M.H. Cho, Y.S. Lee, Novel optical property of SrZrO3 by Cu-ion doping, J. Kor. Phys. Soc. 63 (11) (2013) 2185–2189, https://doi.org/10.3938/jkps.63.2185.

[42] I. Ahemen, F.B. Dejene, Site spectroscopy probing of Eu3+ incorporated into novel LiY Sr ZrO3+α host matrix, Curr. Appl. Phys. 18 (11) (2018) 1359–1367, https://doi.org/10.1016/j.cap.2018.07.021.

[43] K. Sedeek, N. Makram, H. Hantour, T.Z. Amer, S.A. Said, An explicit and novel structure, lattice dynamics, and photoemission of La-doped nanocrystalline SrZrO3 perovskite, Rare Met. 40 (1) (2021) 105–112, https://doi.org/10.1007/s12598-019-01326-y.

[44] T. Schober, Water vapor solubility and impedance of the high temperature proton conductor SrZr0.9Y0.1O2.95, Solid State Ionics 145 (1–4) (2001) 319–324, https://doi.org/10.1016/S0167-2738(01)00926-2.

[45] G.A. Smolenskii, M.P. Petrov, R v Pisarev, Spin-density distribution and electronic structure in fluorides with the perovskite structure (ABF $_3$, where A=Na, Rb; B=Mn, Ni, Co), J. Appl. Phys. 38 (3) (1967) 1269–1271, https://doi.org/10.1063/1.1709573.

[46] Z. Yang, D. Xu, J. Du, X. Gao, J. Sun, Tunable luminescence and energy transfer of a Eu $^{2+}$/Mn $^{2+}$ co-doped Sr $_3$ NaY(PO $_4$) $_3$ F phosphor for white LEDs, RSC Adv. 6 (90) (2016) 87493–87501, https://doi.org/10.1039/C6RA20699A.

[47] J. Lelievre, M. Josse, P. Marchet, Structure and properties of (Na0.5Bi0.5)ZrO3 (NBZ) lead-free perovskite compound, Scripta Mater. 161 (2019) 13–17, https://doi.org/10.1016/j.scriptamat.2018.10.003.

[48] R.W.G. Wyckoff, Crystal structures, Interscience publishers 1 (2) (1963) 238–239.

[49] S.K. Gupta, N. Pathak, R. Gupta, S.K. Thulasidas, V. Natarajan, Probing the oxidation state and coordination geometry of uranium ion in SrZrO3 perovskite, J. Mol. Struct. 1068 (2014) 204–209, https://doi.org/10.1016/j.molstruc.2014.04.016.

[50] S.N. Shkerin, A.V. Rudakova, K.M. Bulanin, et al., Raman spectroscopy of SrZrO3 based proton conducting electrolyte: effect of Y-doping and Sr-nonstoichiometry, Int. J. Hydrogen Energy 46 (32) (2021) 17007–17018, https://doi.org/10.1016/j.ijhydene.2020.11.236.

[51] L.B. McCusker, R.B. von Dreele, D.E. Cox, D. Louër, P. Scardi, Rietveld refinement guidelines, J. Appl. Crystallogr. 32 (1) (1999) 36–50, https://doi.org/10.1107/S0021889898009856.

[52] Z. Huang, P. Thomson, S. Di, Lattice contractions of a nanoparticle due to the surface tension: a model of elasticity, J. Phys. Chem. Solid. 68 (4) (2007) 530–535, https://doi.org/10.1016/j.jpcs.2007.01.016.

[53] C. Shivakumara, R. Saraf, P. Halappa, White luminescence in Dy 3+ doped BiOCl phosphors and their Judd–Ofelt analysis, Dyes Pigments 126 (2016) 154–164, https://doi.org/10.1016/j.dyepig.2015.10.032.

[54] R. Rajesh, S. John Ethilton, K. Ramachandran, N.v Giridharan, K. Ramesh Kumar, S.S. Valath, Studies on multiferroic properties of single phasic Bi $_{0.85}$ Ho $_{0.05}$ Sm $_{0.1}$ FeO $_3$ ceramics, Int. J. Mod. Phys. B 32 (25) (2018), 1850277, https://doi.org/10.1142/S0217979218502776.

[55] P. Redhu, R. Punia, A. Hooda, B.P. Malik, G. Sharma, P. Sharma, Correlation between multifunctional properties of lead free Iron doped BCT perovskite ceramics, Ceram. Int. 46 (11) (2020) 17495–17507, https://doi.org/10.1016/j.ceramint.2020.04.045.

[56] W. Travis, E.N.K. Glover, H. Bronstein, D.O. Scanlon, R.G. Palgrave, On the application of the tolerance factor to inorganic and hybrid halide perovskites: a revised system, Chem. Sci. 7 (7) (2016) 4548–4556, https://doi.org/10.1039/C5SC04845A.

[57] I. Yamada, A. Takamatsu, H. Ikeno, Complementary evaluation of structure stability of perovskite oxides using bond-valence and density-functional-theory calculations, Sci. Technol. Adv. Mater. 19 (1) (2018) 101–107, https://doi.org/10.1080/14686996.2018.1430449.

[58] Kim Jun Ho Yun Jeong Woo, Sulfur tolerance effects on Sr0.92Y0.08Ti0.5Fe0.5O3-δ as an alternative anode in solid oxide fuel cells, J Electrochem Sci Technol 9 (2) (2018) 133–140, https://doi.org/10.5229/JECST.2018.9.2.133.

[59] P.G. Radaelli, G. Iannone, M. Marezio, et al., Structural effects on the magnetic and transport properties of perovskite A1−xAx'MnO3 (x=0.25,0.30), Phys. Rev. B 56 (13) (1997) 8265–8276, https://doi.org/10.1103/PhysRevB.56.8265.

[60] T. Chatterji, B. Ouladdiaf, P. Mandal, B. Bandyopadhyay, B. Ghosh, Jahn-Teller transition in La 1− x Sr x MnO 3 in the low-doping region (0< x<~ 0. 1), Phys. Rev. B 66 (5) (2002), 054403, https://doi.org/10.1103/PhysRevB.66.054403.

[61] Y. Shimakawa, Y. Kubo, Y. Tauchi, T. Kamiyama, H. Asano, F. Izumi, Structural distortion and ferroelectric properties of SrBi2(Ta1−xNbx)2O9, Appl. Phys. Lett. 77 (17) (2000) 2749–2751, https://doi.org/10.1063/1.1319509.

[62] D.L. Wood, J. Tauc, Weak absorption tails in amorphous semiconductors, Phys. Rev. B 5 (8) (1972) 3144–3151, https://doi.org/10.1103/PhysRevB.5.3144.

[63] P.R. Jubu, O.S. Obaseki, A. Nathan-Abutu, F.K. Yam, Y. Yusof, M.B. Ochang, Dispensability of the conventional Tauc's plot for accurate bandgap determination from UV–vis optical diffuse reflectance data, Results in Optics 9 (2022), 100273, https://doi.org/10.1016/j.rio.2022.100273.

[64] M.F.C. Gurgel, J.W.M. Espinosa, A.B. Campos, et al., Photoluminescence of crystalline and disordered BTO:Mn powder: experimental and theoretical modeling, J. Lumin. 126 (2) (2007) 771–778, https://doi.org/10.1016/j.jlumin.2006.11.011.

[65] V.M. Longo, L.S. Cavalcante, R. Erlo, et al., Strong violet–blue light photoluminescence emission at room temperature in SrZrO3: joint experimental and theoretical study, Acta Mater. 56 (10) (2008) 2191–2202, https://doi.org/10.1016/j.actamat.2007.12.059.

[66] L. Weston, A. Janotti, X.Y. Cui, B. Himmetoglu, C. Stampfl, C.G. van de Walle, Structural and electronic properties of SrZrO3 and Sr(Ti,Zr) O3 alloys, Phys. Rev. B 92 (8) (2015), 085201, https://doi.org/10.1103/PhysRevB.92.085201.

[67] S.S.A. Gillani, R. Ahmad, M. Rizwan, et al., Effect of magnesium doping on band gap and optical properties of SrZrO3 perovskite: a first-principles study, Optik 191 (2019) 132–138, https://doi.org/10.1016/j.ijleo.2019.05.099.

[68] M. Rizwan, S. Anam, M. Farman, A. Akgul, M. Uzma, Role of Zn in modification of electronic and optical properties of c-SrZrO $_3$: a computational insight, Phys. Scripta 95 (8) (2020), 085212, https://doi.org/10.1088/1402-4896/ab9f7b.

[69] S. Chettri, D.P. Rai, A. Shankar, M.P. Ghimire, R. Khenata, R.K. Thapa, A systematic study of LaAlO $_3$ with variation of Nd doping, case of band gap tuning: a first principles method, Mod. Phys. Lett. B 30 (4) (2016) 1650028, https://doi.org/10.1142/S0217984916500287.

[70] L. Zhang, J. Wang, D. Peng, et al., Photoluminescence and dielectric properties of pure/Yb-doped SrZrO 3 crystals, J. Phys. Chem. Solid. 104 (2017) 1–7, https://doi.org/10.1016/j.jpcs.2017.01.002.

[71] L.S. Cavalcante, V.M. Longo, M. Zampieri, et al., Experimental and theoretical correlation of very intense visible green photoluminescence in BaZrO3 powders, J. Appl. Phys. 103 (6) (2008), 063527, https://doi.org/10.1063/1.2901176.

[72] F. Shi, K. Liang, Z.M. Qi, Investigation of the crystal structure, lattice vibration and dielectric property of SrZrO $_3$ ceramic, J. Mater. Res. 31 (20) (2016) 3249–3254, https://doi.org/10.1557/jmr.2016.340.

[73] E. Fernández López, V. Sánchez Escribano, M. Panizza, M.M. Carnasciali, G. Busca, Vibrational and electronic spectroscopic properties of zirconia powders, J. Mater. Chem. 11 (7) (2001) 1891–1897, https://doi.org/10.1039/b100909p.

[74] X. Li, W. Ma, J. Wen, et al., Preparation of SrZrO3 thermal barrier coating by solution precursor plasma spray, J. Therm. Spray Technol. 26 (3) (2017) 371–377, https://doi.org/10.1007/s11666-017-0527-8.

[75] L.S. Cavalcante, A.Z. Simões, J.C. Sczancoski, et al., SrZrO3 powders obtained by chemical method: synthesis, characterization and optical absorption behaviour, Solid State Sci. 9 (11) (2007) 1020–1027, https://doi.org/10.1016/j.solidstatesciences.2007.07.019.

[76] M. Tarrida, H. Larguem, M. Madon, Structural investigations of (Ca,Sr)ZrO3 and Ca (Sn,Zr)O3 perovskite compounds, Phys. Chem. Miner. 36 (7) (2009) 403–413, https://doi.org/10.1007/s00269-008-0286-7.

[77] M. O'Keeffe, B.G. Hyde, Some structures topologically related to cubic perovskite ($E\,2_1$), ReO$_3$ ($D\,0_9$) and Cu$_3$ Au ($L\,1_2$), Acta Crystallogr. B 33 (12) (1977) 3802–3813, https://doi.org/10.1107/S0567740877012114.

[78] M. Shivaram, H. Nagabhushana, S.C. Sharma, et al., Synthesis and luminescence properties of Sm3+ doped CaTiO3 nanophosphor for application in white LED under NUV excitation, Spectrochim. Acta Mol. Biomol. Spectrosc. 128 (2014) 891–901, https://doi.org/10.1016/j.saa.2014.02.117.

[79] A. Chopelas, Single-crystal Raman spectra of YAlO3 and GdAlO3: comparison to several orthorhombic ABO3 perovskites, Phys. Chem. Miner. 38 (9) (2011) 709–726, https://doi.org/10.1007/s00269-011-0444-1.

[80] O. Kamishima, T. Hattori, K. Ohta, Y. Chiba, M. Ishigame, Raman scattering of single-crystal SrZrOsub3/sub, J. Phys. Condens. Matter 11 (27) (1999) 5355–5365, https://doi.org/10.1088/0953-8984/11/27/311.

[81] A. Slodczyk, M.H. Limage, P. Colomban, et al., Substitution and proton doping effect on SrZrO$_3$ behaviour: high-pressure Raman study, J. Raman Spectrosc. 42 (12) (2011) 2089–2099, https://doi.org/10.1002/jrs.2968.

[82] S. Amisi, E. Bousquet, K. Katcho, P. Ghosez, First-principles study of structural and vibrational properties of SrZrO3, Phys. Rev. B 85 (6) (2012), 064112, https://doi.org/10.1103/PhysRevB.85.064112.

[83] D. Gazzoli, G. Mattei, M. Valigi, Raman and X-ray investigations of the incorporation of Ca2+ and Cd2+ in the ZrO2 structure, J. Raman Spectrosc. 38 (7) (2007) 824–831, https://doi.org/10.1002/jrs.1708.

[84] S. Kumar, S. Bhunia, A.K. Ojha, Effect of calcination temperature on phase transformation, structural and optical properties of sol–gel derived ZrO2 nanostructures, Physica E Low Dimens Syst Nanostruct 66 (2015) 74–80, https://doi.org/10.1016/j.physe.2014.09.007.

[85] Z. Liu, W. Ji, L. Dong, Y. Chen, Effect of supported Na+Ions on the texture properties of ZrO2, J. Solid State Chem. 138 (1) (1998) 41–46, https://doi.org/10.1006/jssc.1998.7752.

[86] A. Sarakovskis, J. Grube, A. Mishnev, M. Springis, Up-conversion processes in NaLaF4:Er3+, Opt. Mater. 31 (10) (2009) 1517–1524, https://doi.org/10.1016/j.optmat.2009.02.015.

[87] S. Das, C.Y. Yang, C.H. Lu, Structural and optical properties of tunable warm-white light-emitting ZrO$_2$:Dy^{3+} -Eu^{3+} nanocrystals, J. Am. Ceram. Soc. 96 (5) (2013) 1602–1609, https://doi.org/10.1111/jace.12149.

[88] A. Zhang, M. Lü, S. Wang, G. Zhou, S. Wang, Y. Zhou, Novel photoluminescence of SrZrO3 nanocrystals synthesized through a facile combustion method, J. Alloys Compd. 433 (1–2) (2007) L7–L11, https://doi.org/10.1016/j.jallcom.2006.06.083.

[89] V.M. Longo, L.S. Cavalcante, M.G.S. Costa, et al., First principles calculations on the origin of violet-blue and green light photoluminescence emission in SrZrO3 and SrTiO3 perovskites, Theor. Chem. Acc. 124 (5–6) (2009) 385–394, https://doi.org/10.1007/s00214-009-0628-7.

[90] D.J. Lee, D.H. Kim, J.W. Park, Y.S. Lee, Room-temperature violet-blue emission for SrZrO3 nanocrystals synthesized by using the combustion method, J. Kor. Phys. Soc. 59 (4) (2011) 2797–2800, https://doi.org/10.3938/jkps.59.2797.

[91] J.W. Park, D.J. Lee, D.H. Kim, Y. Lee, Low-temperature photoluminescence for polycrystalline SrZrO3 and SrHfO3, J. Kor. Phys. Soc. 58 (2) (2011) 316–320, https://doi.org/10.3938/jkps.58.316.

[92] B. Evangeline, P.A. Azeem, R. Prasada Rao, G. Swati, D. Haranath, Structural and luminescent features of cerium doped CaZrO3 blue nanophosphors, J. Alloys Compd. 705 (2017) 618–623, https://doi.org/10.1016/j.jallcom.2016.11.115.

[93] S.K. Sharma, S. Som, R. Jain, A.K. Kunti, Spectral and CIE parameters of red emitting Gd3Ga5O12:Eu3+ phosphor, J. Lumin. 159 (2015) 317–324, https://doi.org/10.1016/j.jlumin.2014.11.010.